AIAA JOURNAL
Vol. 43, No. 10, October 2005

# Three-Dimensional Normal Shock-Wave/Boundary-Layer Interaction in a Rectangular Duct

Taro Handa* and Mitsuharu Masuda†
*Kyushu University, Fukuoka 816-8580, Japan*
and
Kazuyasu Matsuo‡
*University of Kitakyushu, Fukuoka 808-0135, Japan*

**The three-dimensional flow structure induced by normal shock-wave/turbulent boundary-layer interaction in a constant-area rectangular duct is investigated by a laser-induced-fluorescence method. This diagnostic system uses an argon-ion laser as a light source, and the target gas is dry nitrogen with iodine seeded as a fluorescence material. The Mach-number distributions in the duct are obtained from the measured fluorescence intensity, and the three-dimensional flow pattern in the expansion region downstream of the initial shock wave is clarified. In addition to this, the region having locally higher Mach number near the duct corners is observed immediately behind the shock wave, and the three-dimensional shape of the boundary layers is found. These flow characteristics are reproduced by solving the Navier–Stokes equations numerically. The calculated result reveals that the complicated shock-wave configuration is formed at the duct corner because of the interaction of two bifurcated shock waves developed on the two perpendicularly adjacent walls. The simple flow model is also constructed by considering this interaction. This model can explain very well the three-dimensional flow characteristics.**

## Introduction

NORMAL shock-wave/turbulent boundary-layer interaction (NSW/TBLI) generated in supersonic flows in a rectangular duct appears in various high-speed flow devices, for example, inlets of the airbreathing engine, supersonic ejectors, compressor cascades, and supersonic nozzles. This interaction generates a highly three-dimensional flow structure as a result of the four flat walls enclosing the duct and influences the aerodynamic performance of the systems. Although the three-dimensional characteristics are important in engineering applications, not much work has been done on this problem.

Doerffer and Dallmann[1] investigated the three-dimensional characteristics of the flow with NSW/TBLI on a convex wall in a wind tunnel at a Mach number of 1.47. They controlled the boundary-layer thickness and changed the Reynolds number based on the boundary-layer thickness. They found that asymmetry of the oil-flow pattern increased substantially with Reynolds number. This indicated that a streamwise helical flow existed downstream of the shock wave.

Bejm et al.[2] made another experimental investigation with the same facility as Doerffer and Dallmann. They used two curved passages having the same shape but different span. Their oil-flow visualization results suggested that the three-dimensional flow characteristics depended strongly on the span.

Gerolymos et al.[3] described the three-dimensional character of the flow produced by the NSW/TBLI at the corners of a nozzle with rectangular cross section by solving Navier–Stokes equations with the $k$–$\varepsilon$ two-equation turbulence model. In their numerical results, a three-dimensional recirculation zone appeared in the corners. However, this zone was not verified because they did not have three-dimensional experimental data to be compared with their calculation.

Chriss et al.[4] investigated the three-dimensional nature of the NSW/TBLI flows in a constant area rectangular duct by using a laser Doppler velocimetry method. They tested inlet Mach numbers of 1.28 and 1.59. They found that the flow for the inlet Mach number of 1.59 had the local region having higher Mach number at the duct corners behind the initial shock wave. However, they did not describe the reason of this region. The flow for the inlet Mach number of 1.28 had a weak three dimensionality.

In spite of work just described, important questions remain unsolved. These are, first, what is the three-dimensional character of an internal flow with NSW/TBLI?; second, how is that flow generated?; finally, what shape does a shock wave at the corner of a duct take? To answer these, we studied the flow in a rectangular duct. The cross-sectional area of the duct was taken constant because the fundamental interaction phenomenon could be observed without the effect of the change in flow area.

In the present work, three-dimensional distributions of flowfield parameters were measured by a laser-induced-fluorescence (LIF) method. This diagnostic system uses an argon-ion laser with iodine seeded as a fluorescence material. When the pressure of the flow is nearly atmospheric, the rate of collisional quenching of iodine molecules excited by an argon-ion laser dominates that of the spontaneous emission. In this pressure range, the LIF signal intensity is found to depend only on temperature under the condition that an argon-ion laser is operated by the broadband mode with a wavelength of 514.5 nm and that the laser intensity is much less than the saturation intensity.[5–8] This indicates that the temperature distribution can be obtained from the LIF signal if the temperature of one specified point in the flow field is known. In this work, the temperature is converted to the Mach number by assuming the flow being adiabatic because the Mach number is more useful to analyze the flow characteristics than temperature.

In the present experiment, the laser beam sheet was injected into the duct from the downstream direction. The laser beam sheet was scanned across the flowfield, and the two-dimensional LIF image of each scan was recorded by a charge-coupled-device (CCD) camera. The image data were stored into the computer, and the three-dimensional distribution of Mach number was calculated. With this method, the complicated flowfield in the duct was clarified including

---

Received 23 August 2004; revision received 27 February 2005; accepted for publication 1 March 2005.

*Associate Professor, Department of Energy and Environmental Engineering, 6-1 Kasuga-Koen, Kasuga City; handa@ence.kyushu-u.ac.jp.

†Professor, Department of Energy and Environmental Engineering, 6-1 Kasuga-Koen, Kasuga City; masuda@ence.kyushu-u.ac.jp.

‡Professor, Department of Mechanical Systems and Environmental Engineering, 1-1 Hibikino, Wakamatsu-ku, Kitakyushu City; matsuo@env.kitakyu-u.ac.jp.

the three-dimensional pattern of the boundary-layer separation induced by a shock wave. To investigate the reliability of the measurement and consider the flowfield in detail, a Navier–Stokes flow simulation with $k$–$\omega$ two-equation turbulence model was performed, and the computed results were compared with experiments.

## Diagnostic System

When iodine molecules are excited by an argon-ion laser lasing with a broadband mode of 514.5-nm wavelength and with the power much lower than the saturation intensity, the LIF intensity $S_F$ is given as[5–8]

$$S_F = C\left[f(T)\big/\sqrt{T}\,\right] \tag{1}$$

In the preceding equation, $C$ is a constant, and $f(T)$ is the population fraction of iodine molecules that depends only on temperature $T$. This equation is derived by assuming that the spontaneous emission coefficient is much smaller than the collisional quenching rate. This assumption is achieved when pressure is larger than 20 kPa (Ref. 7).

Equation (1) indicates that the LIF intensity depends only on temperature. Therefore, if the temperature and the LIF intensity are known at one specified point in the flowfield, the constant $C$ is evaluated, and LIF intensity distribution gives the temperature distribution of the flowfield. In the calculation of $f(T)$, the quantum numbers taken into account are 0, 1, and 2 for the vibrational and 13 and 15 for the rotational quantum energy states, respectively.

In the flowfield of polyatomic gases with high expansion rate, the flow cannot maintain an equilibrium state, and the difference can occur among the translational, rotational, and vibrational temperatures.[9] In this situation, the temperature obtained by LIF method is questionable. However, in the present experiment the expansion of the gas is constrained by the walls of a duct, and the maximum Mach number is less than 1.7, so that the nonequilibrium effect can be neglected.

In the present paper, a Mach-number distribution is obtained from the temperature measured by a LIF method. To calculate Mach number from temperature, the stagnation temperature is taken as constant over the entire flowfield, that is, the flow is assumed adiabatic. This approximation was experimentally verified in transonic and supersonic internal flows.[10,11] Mach number $M$ is then calculated by the following equation:

$$T_0/T = 1 + [(\gamma - 1)/2]M^2 \tag{2}$$

where $T_0$ and $\gamma$ are stagnation temperature and specific heat ratio, respectively.

The experimental setup are shown in Fig. 1, where 1–5 correspond to the LIF diagnostic system. The laser is an argon-ion laser (Spectra Physics, Model 2017, 5 W) with a prism in the cavity and is lased with a broadband mode of 514.5-nm wavelength. The laser beam is shaped to a sheet with a thickness of 0.5 mm through one convex lens (15-mm focal length) and two cylindrical lenses (100- and 1000-mm focal lengths) (3), and it is injected into the duct from the downstream direction. The resulting LIF signal is measured from the direction perpendicular to the laser sheet. The signal is collected by a lens (Nikon, F 1.4) and detected by the CCD camera with image intensifier (Hamamatsu Photonics C7772S) (4). The laser collimation and collection optics are moved to scan along the depth direction of the duct, and the LIF images for each scan is stored in the computer. With this procedure, the three-dimensional distribution of the LIF intensity is obtained, and the Mach-number distribution on a specified plane is analyzed.

The sensitivity of an image intensifier is not uniform over the plane of its output phosphor. Also, as a result of the upper and lower walls of the duct, the solid angle of the LIF collection optics is not the same for images taken at the different location. To take these effects into account, the diagnostic system is calibrated by filling the still air with an iodine seed in the duct. This still air is irradiated by the laser, and by scanning the optical system the LIF signals are recorded for each plane where the LIF image of the flowfield is to be taken. By using these as reference images, the image data of the flowfield are corrected.

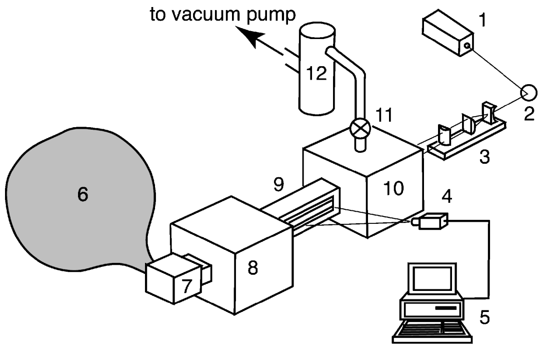

**Fig. 1 Experimental setup: 1) Ar laser, 2) mirror, 3) cylindrical lenses, 4) CCD camera, 5) personal computer, 6) balloon, 7) iodine cell, 8) stagnation chamber, 9) test duct, 10) expansion chamber, 11) valve, and 12) vacuum tank.**

The spatial resolution of the present diagnostic system is determined by the thickness of the laser beam sheet in the depth direction and is less than 0.5 mm. On the image plane, the simple geometrical consideration shows that the one pixel of the image plane corresponds to the physical size of 0.11 × 0.11 mm. To estimate the resolution accurately, however, it is necessary to clarify the integrated resolution including the characteristics of collection optics, the image intensifier, the CCD camera, and the frame digitizer in the computer. Therefore, we made an experiment similar to that done by McMillin et al.[12] and took the image of a knife edge. According to this experiment, the image of the knife edge is found to be recorded in four pixels, so that the one pixel corresponds to the 0.44 × 0.44 mm. The temporal resolution is limited by the framing rate of the CCD camera and is 1/30 s.

Inoue et al. checked the accuracy of the temperature measurement with the same diagnostic system by using the flow in a two-dimensional transonic nozzle.[5,6] The temperatures obtained by the LIF method were compared with those calculated from the measured values of the stagnation and static pressures on the nozzle side wall by assuming the flow being adiabatic. Both values agree within ±3.0 K, which correspond to Mach number of ±0.038. The range of flow parameters in the present experiment is almost identical with this calibration experiment, so that the similar accuracy is obtained in the present duct flow.

## Experimental Setup and Method

The experimental setup is shown by 6–12 of Fig. 1. The wind tunnel is a blowdown type operated by dry nitrogen with atmospheric pressure and temperature. The dry nitrogen has water content less than 5 ppm, and the condensation in the duct is avoided by using this gas. The vacuum tank (12) in Fig. 1 is evacuated to a pressure less than 13 kPa by closing the valve (11), and then the dry nitrogen contained in the balloon (6) is introduced into the iodine cell (7), where iodine is sublimated into nitrogen. Nitrogen with a small amount of iodine (~4 wt%) is supplied to the test duct (9) through the stagnation chamber (8). The duration of the wind tunnel is limited by the pressure increase of the vacuum tank and is about 60 s. The pressure and temperature in the stagnation chamber are maintained at $1.012 \times 10^5$ Pa and 293.3 K, respectively.

Figure 2 shows the detailed structure of the test duct. The Mach number at the entrance of a constant-area cross section is 1.68. This value is calculated from the time-averaged static pressure on the side wall and the stagnation pressure in the plenum chamber. The coordinate used to analyze results is defined in Fig. 3, where $x$, $y$, and $z$ are the streamwise, height, and depth coordinates, respectively.

The flowfield is scanned in the depth direction from $z = -9.5$ to 9.5 mm with a step of 1 mm by the laser sheet formed parallel to the $x$–$y$ plane. It takes at least 1/30 s to obtain the LIF image data for one scan. In the present experiment, however, the pressure is nearly atmospheric. This means that the collisional quenching of the excited iodine molecule is large, resulting in the low LIF intensity. Therefore, the one LIF image taken in 1/30 s is degraded

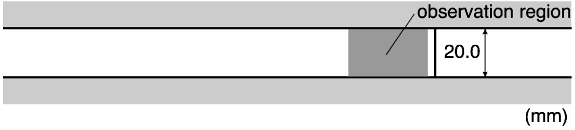

a) Top view

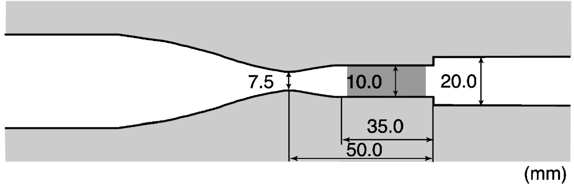

b) Side view

Fig. 2 Test duct.

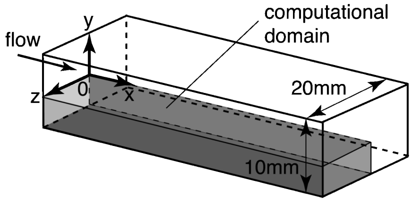

Fig. 3 Coordinate system.

by the noise caused by the photon statistics. To avoid this problem, 10 images are taken successively for each one physical plane and are averaged. Very clear images are obtained by this procedure.

As described earlier, the temperature of the one specified point should be known to obtain its distributions over the whole flowfield. In the present experiment, this point is taken at $x = 3$ mm, $y = 0$, and $z = 7.5$ mm, and the reference temperature is calculated from the time-averaged static pressure on the side wall, the stagnation pressure, and the stagnation temperature in the plenum chamber.

## Numerical Analysis

To investigate the accuracy of Mach-number measurement by the present LIF method, we perform a numerical flow simulation. The governing equations are three-dimensional, Reynolds-averaged Navier–Stokes equations. The inviscid fluxes are evaluated by using a high-resolution upwind scheme based on a total-variation-diminishing (TVD) formulation in which the Roe's approximate Riemann solver[13] and the MUSCL approach with the van Albada limiter are implemented.[14] This scheme has a third-order accuracy in space. The viscous fluxes are determined in a second-order central difference scheme, and the $k$–$\omega$ two-equation turbulence model proposed by Wilcox[15] is employed to estimate the eddy viscosity. This model is modified for the effects of compressibility.[16] The time integration is performed by the three-stage Runge–Kutta method. In the time-integration process, we employ the local time step at each grid point to achieve faster convergence to the steady state.[17]

The computational domain for the present simulation is shown in Fig. 3. It is limited to a quarter of the duct and discretized with $100 \times 50 \times 56$ grid points in the streamwise, height, and depth directions, respectively. We checked the dependence of the solution on the number of grid points by calculating the flow with $80 \times 39 \times 44$ grid points. No discernible difference was observed between these two results. The inlet condition was determined by the preliminary calculation of the flow from the nozzle to the test section. The calculated values on the $y$–$z$ plane at $x = 2$ mm are adopted as an inlet condition. This location is the same as the inlet boundary of the computational domain shown in Fig. 3 and also corresponds to the inlet of the observation region shown in Fig. 2. The stagnation pressure and temperature are set at $1.012 \times 10^5$ Pa and 293.3 K, respectively. In the exit section, static pressure is adjusted to locate the shock wave in the proper position. A no-slip boundary condition is applied on the walls. The velocity perpendicular to the plane is set to zero on the symmetric boundary.

## Results and Discussion

Figure 4 shows measured and computed Mach-number contours on the $x$–$y$ plane at $z = 0.5$ mm. This is near the central part of the duct. The contour step is 0.1. In Fig. 4a, a subsonic region is observed in the downstream of $x \sim 10$ mm. The initial normal shock wave stands at this location, and a flow is decelerated through it to subsonic speed. The deceleration through the normal shock wave is seen gradually because the flow is probably unsteady and the shock wave oscillates in the streamwise direction. The initial shock wave is also observed in the computed result of Fig. 4b. This wave, however, is sharp and bifurcated near the wall because the computed result corresponds to the steady-state solution and the shock wave does not oscillate.

Figure 5 is the sketch of the flow reaccelaration process downstream of the first and second shock waves. This was depicted from the LDV measurement by Carroll and Dutton.[18] The boundary layer at the foot of the first shock-wave thickens because of its strong adverse pressure gradient. Consequently the shock wave becomes bifurcated, and a slip line is developed from the triple point. They emphasized that two different processes cause the initial expansion immediately behind the first shock wave. These are the core-flow aerodynamic nozzle effect caused by the slightly oblique nature of the normal part of the shock wave, and the near-wall displacement thickness effect that accelerates the supersonic flow through an expansion fan shown in Fig. 5. The flow accelerated through these two processes is decelerated again by the second shock wave.

The reacceleration processes just described are well reproduced in the present results in Fig. 4. The supersonic region downstream of the first shock wave can be seen in both experiment and computation. The deceleration process across the second shock wave is also observed in both results. This comparison indicates that the flow near the central plane of the duct is almost two dimensional as shown by an extensive previous literature.

Figures 6 and 7 show measured and computed Mach-number contours, respectively, on the $x$–$z$ plane. These results demonstrate

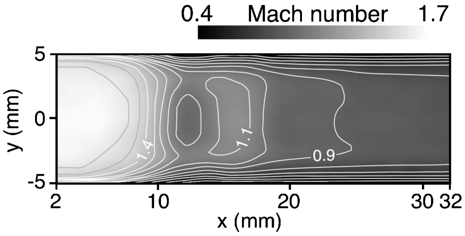

a) Experiment

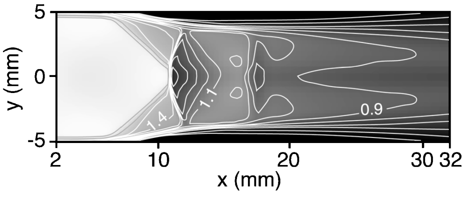

b) Computation

Fig. 4 Mach-number contours on the $x$–$y$ plane at $z = 0.5$ mm.

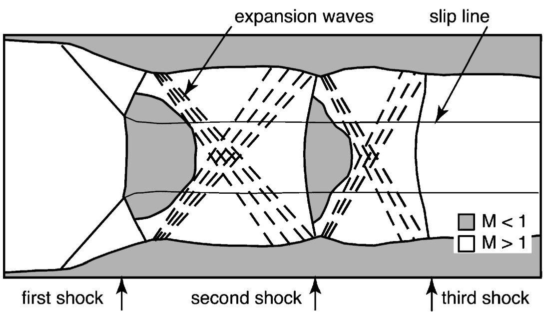

Fig. 5 Sketch of the flow reacceleration process downstream of the first and second shock waves (reproduced from Ref. 18).

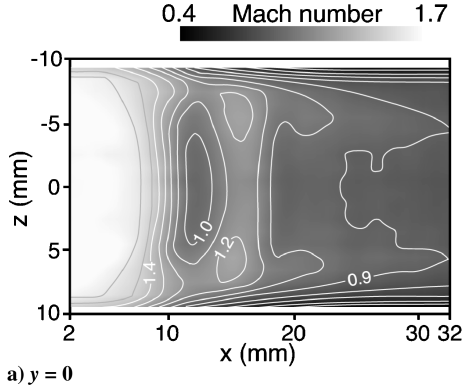

**a)** $y = 0$

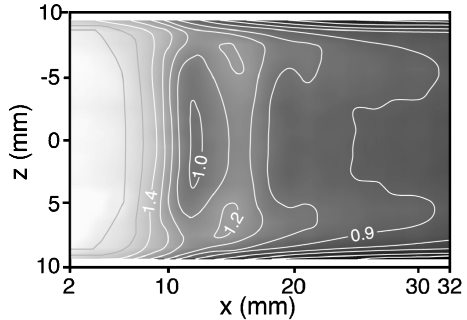

**b)** $y = -2.0$ **mm**

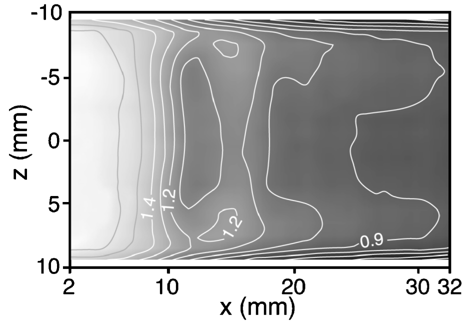

**c)** $y = -2.5$ **mm**

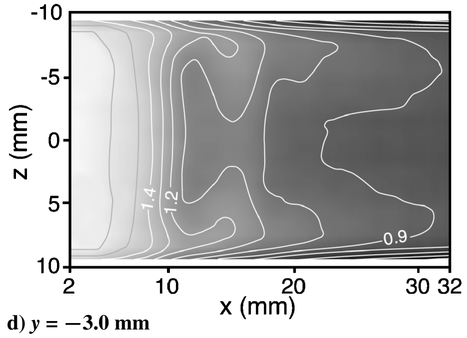

**d)** $y = -3.0$ **mm**

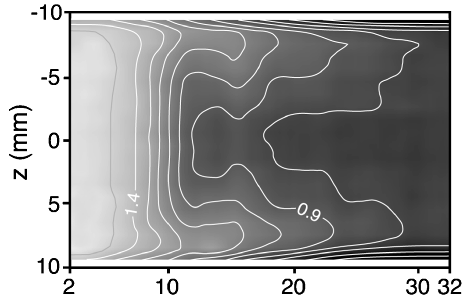

**e)** $y = -4.0$ **mm**

**Fig. 6 Experimental Mach-number contours on the *x–z* plane.**

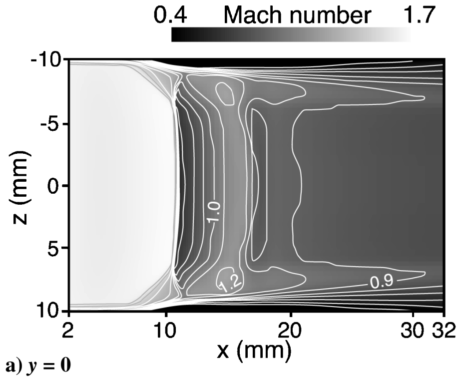

**a)** $y = 0$

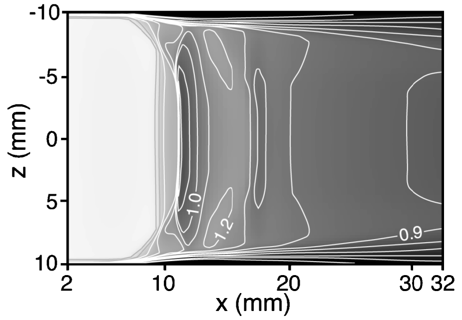

**b)** $y = -2.0$ **mm**

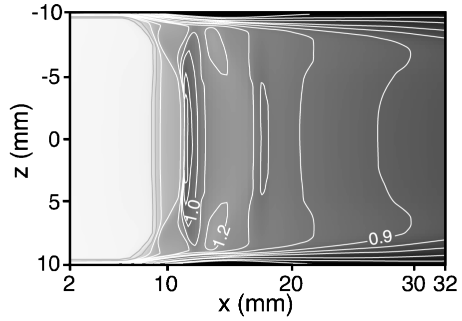

**c)** $y = -2.5$ **mm**

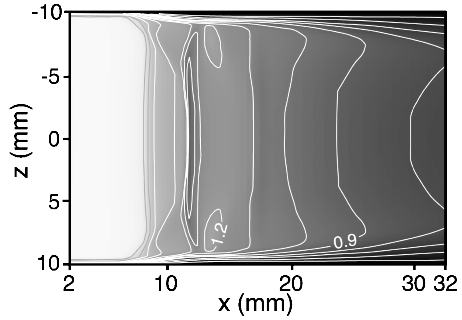

**d)** $y = -3.0$ **mm**

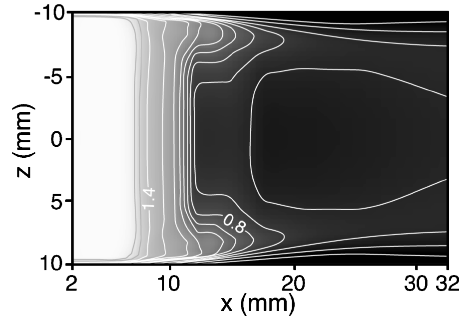

**e)** $y = -4.0$ **mm**

**Fig. 7 Computed Mach-number contours on the *x–z* plane.**

clearly the highly three-dimensional nature of the flowfield. In the experimental result of Fig. 6a, two regions having locally higher Mach number enclosed with the contour of $M = 1.2$ are observed in the downstream of the initial shock wave. These regions become small, move upstream, and approach to the side wall with the decrease of $y$ for $y \geq -2.5$ mm (Figs. 6a–6c). These then merge into the upstream higher-Mach-number region at $y = -3.0$ mm (Fig. 6d). Finally the contour takes the form like two horns at $y = -4.0$ mm (Fig. 6e). Similar patterns are observed in the computed results of Fig. 7.

This flowfield can be explained by the expansion fans shown in Fig. 5. The expansion fans developed on the two perpendicularly adjacent walls overlap and become strong near the duct corner. As a result, the flow in the overlapped region is accelerated, and the Mach number in this region becomes higher than that in the other regions.

Figure 8 shows the measured and computed Mach-number contours immediately behind the initial shock wave. In both results, the higher-Mach-number regions enclosed by the contour of 1.2 exist at four corners of the duct. Similar regions were observed in the measurement of Chriss et al.,[4] but they did not explain this phenomenon. Figure 8 also shows that the boundary layers near a duct corner are thin compared with those on a wall near the duct center.

To explain the three-dimensional characteristics just described, the computed shock-wave structure at a duct corner is examined in detail. This structure is clearly visualized by the streamwise pressure gradient as shown in Fig. 9. The black color shows the large positive pressure gradient and corresponds to a compression or shock wave. The waves A and B in the figure are a front leg of the bifurcated shock wave on the side and bottom walls, respectively. The wave C is a rear leg generated by the requirement that the pressure behind the initial shock wave must be uniform over an entire cross section of the duct. For $z = 5.5$–$7.5$ mm, wave A is observed between waves B and C, and the resulting shock-wave structure takes complicated configurations. The existence of the wave A has not been expected so far. It seems, however, difficult to prove this wave experimentally because the shock-wave system in the duct is usually oscillating.

With the results shown in Fig. 9, the wave structure near a duct corner is modeled, as shown by Fig. 10. On plane A away from the side wall, the shock wave takes a normal λ shape. At the corner of a duct, on the other hand, the bifurcated shock wave developed on a lower wall interacts with that on a side wall, and the wave configuration on plane B near the side wall becomes complicated. On plane A, a flow near the lower wall passes through two bifurcated oblique shock waves (path a), whereas the flow in a corner region passes three oblique shock waves (path b). The Mach number behind the terminal oblique shock wave is determined by the condition that the static pressure at this location must be uniform over the entire cross section of the duct. This condition dictates that the adverse pressure gradient across the two oblique shock waves along path a on plane A becomes large compared with that across the three oblique shock waves along path b on plane B. As a result, the boundary layer at the stem of the terminal oblique shock wave on plane A becomes thicker than that on plane B. This consideration explains that the corner boundary layer shown in Fig. 8 is thin compared with that in the duct center.

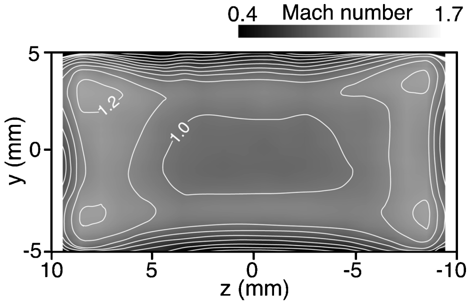

**a) Experiment**

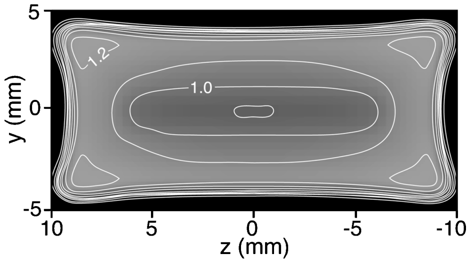

**b) Computation**

**Fig. 8 Mach-number contours behind the initial shock wave ($y$–$z$ plane).**

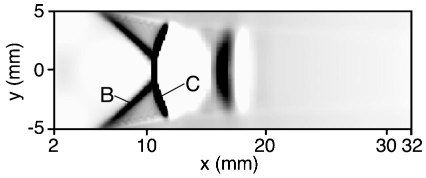

**a) $z = 5.0$ mm**

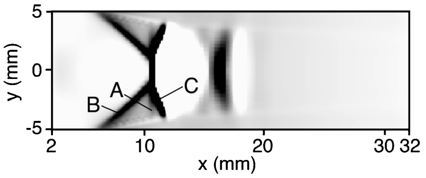

**b) $z = 5.5$ mm**

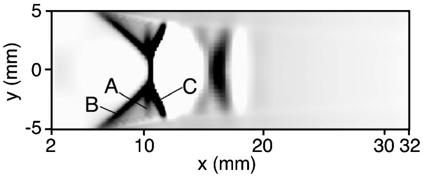

**c) $z = 6.0$ mm**

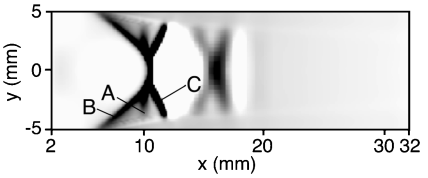

**d) $z = 6.5$ mm**

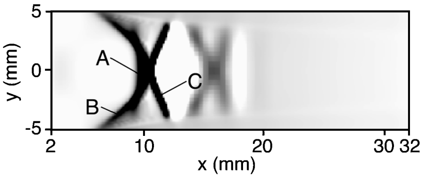

**e) $z = 7.5$ mm**

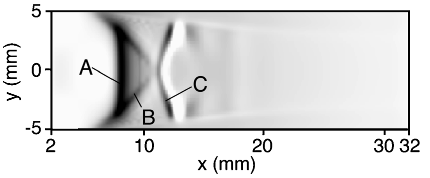

**f) $z = 9.0$ mm**

**Fig. 9 Streamwise pressure gradient on the $x$–$y$ plane.**

For the shock system model assumed in Fig. 10, the simple adiabatic flow theory[19] can give the Mach-number distribution behind the initial shock wave. In the calculation, the displacement effect of the boundary layer is simulated by a wedge placed on the wall. The inlet Mach number and apex angle of the wedge are assumed as 1.68 and 5.0 deg, respectively. The results are shown in Fig. 11.

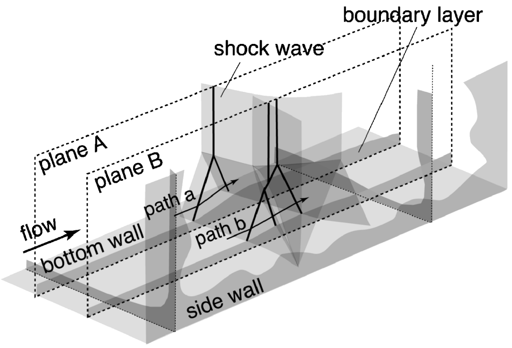

**Fig. 10 Shock system model near a duct corner.**

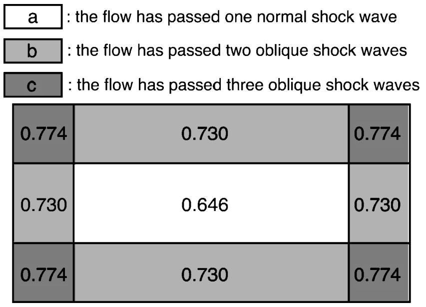

a : the flow has passed one normal shock wave
b : the flow has passed two oblique shock waves
c : the flow has passed three oblique shock waves

| | | |
|---|---|---|
| 0.774 | 0.730 | 0.774 |
| 0.730 | 0.646 | 0.730 |
| 0.774 | 0.730 | 0.774 |

**Fig. 11 Calculated Mach numbers over the duct cross section behind the initial shock wave. (The inlet Mach number and the flow deflection angle on the wall are set at 1.68 and 5.0 deg.)**

According to the shock system model of Fig. 10, the flow is divided into three regions. Regions a, b, and c correspond to the flow that the fluid has passed one normal shock wave, two oblique shock waves, and three oblique shock waves, respectively. As shown in Fig. 11, the Mach number near a duct corner becomes high compared to the other part of the flow. This shows that the present simple flow model explains the experimental result qualitatively well. The experimental Mach number at the duct corner, however, is high compared with this calculation. This discrepancy is probably caused by that; this model takes only the deceleration process of the flow across the shock waves into account and neglects the expansion process caused by the effect of the boundary layer.

## Conclusions

Three-dimensional flow structure of normal shock-wave/turbulent boundary-layer interaction (NSW/TBLI) in a constant-area rectangular duct was investigated by the laser-induced-fluorescence method. This system used the argon-ion laser as a light source, and the target gas was dry nitrogen seeded with iodine. By this method, the temperature distribution in the flow was obtained, and it was converted to the Mach number with the assumption of an adiabatic flow.

The results revealed that the flow induced by NSW/TBLI was complicated and highly three dimensional. It was found that the Mach number immediately downstream of the initial shock wave was not uniform over the duct cross section; the Mach number in the four corner regions of the duct was higher than the central part. The boundary layer near the corner was also found thin compared with that on the wall near the duct center.

The numerical analysis was also carried out by solving the three-dimensional, Reynolds-averaged Navier–Stokes equations. Because of the oscillation of the shock waves in the experiment, Mach-number contour obtained by the experiment was not so clear as those by the calculation; nevertheless, the quantitatively good agreement was obtained between the experiment and the calculation. The calculation also clarified the complicated shock-wave system in the duct corner, and it was found that this configuration was formed by the interaction between two bifurcated shock waves developed on two perpendicularly adjacent walls.

The simple model was made for this shock-wave system. This enabled the calculation of the flow properties by the simple adiabatic flow relations and explained qualitatively the nonuniformity of the Mach-number distribution over the duct cross section behind the initial shock wave.

These results, we believe, give the answers to the questions posed in the Introduction.

## Acknowledgments

The authors express their thanks to J. C. Dutton and E. Loth of University of Illinois for their valuable advice and are grateful to H. Nishida and Y. Ikushima for their assistance in the experimental work.

## References

[1] Doerffer, P., and Dallmann, U., "Reynolds Number Effect on Separation Structures at Normal Shock Wave/Turbulent Boundary-Layer Interaction," *AIAA Journal*, Vol. 27, No. 9, 1989, pp. 1206–1212.

[2] Bejm, M., Doerffer, P., and Kania, W., "An Effect of Test Section Span on the Shock Wave—Turbulent Boundary Layer Interaction," *4th International Symposium on Experimental and Computational Aerothermodynamics of Internal Flows*, Vol. 1, 1999, pp. 102–110.

[3] Gerolymos, G. A., Vallet, I., Bölcs, A., and Ott, P., "Computation of Unsteady Three-Dimensional Transonic Nozzle Flows Using $k$–$\varepsilon$ Turbulence Closure," *AIAA Journal*, Vol. 34, No. 7, 1996, pp. 1331–1340.

[4] Chriss, R. M., Hingst, W. R., Strazisar, A. J., and Keith, T. G., "An LDA Investigation of the Normal Shock Wave Boundary Layer Interaction," *La Recherche Aérospatiale*, No. 1990-2, 1990, pp. 1–15.

[5] Inoue, M., Muraishi, T., Masuda, M., and Natsunari, K., "Visualization of Transonic Flow in Curved Nozzle with Rectangular Cross-Section by Laser-Induced Fluorescence Method," *Journal of the Visualization Society of Japan*, Vol. 10, Suppl. 2, 1990, pp. 103–106 (in Japanese).

[6] Inoue, M., Masuda, M., and Muraishi, T., "Visualization of Transonic Nozzle Flow by Laser-Induced Fluorescence Method," *Journal of the Visualization Society of Japan*, Vol. 11, Suppl. 2, 1991, pp. 35–38 (in Japanese).

[7] Hartfield, R. J., Hollo, S. D., and McDaniel, J. C., "Planar Temperature Measurement in Compressible Flows Using Laser-Induced Fluorescence," *Optics Letters*, Vol. 16, No. 2, 1991, pp. 106–108.

[8] Inoue, M., Masuda, M., Furukawa, M., and Muraishi, T., "Diagnosis of Three-Dimensional Transonic Flow Fields with Laser-Induced Iodine Fluorescence," *Proceedings of the 1995 ASME/JSME Fluids Engineering and Laser Anemometry Conference; Experimental and Numerical Flow Visualization*, FED-Vol. 218, edited by B. Khalighi, T. Kobayashi, D. H. Fruman, M. J. Braun, C. J. Freitas, and F. Baban, American Society of Mechanical Engineers, New York, 1995, pp. 163–170.

[9] Soga, T., and Niwa, K., "On the Rotational and Transrational Nonequilibrium in an Under-Expanded Free Jet of Nitrogen," *Transactions of the Japan Society for Aeronautical and Space Sciences*, Vol. 28, No. 79, 1985, pp. 16–26.

[10] Carroll, B. F., Lopez-Fernandez, P. A., and Dutton, J. C., "Computations and Experiments for a Multiple Normal Shock/Boundary-Layer Interaction," *Journal of Propulsion and Power*, Vol. 9, No. 3, 1993, pp. 405–411.

[11] Cahen, J., Couaillier, V., Délery, J., and Pot, T., "Validation of Code Using Turbulence Model Applied to Three-Dimensional Transonic Channel," *AIAA Journal*, Vol. 33, No. 4, 1995, pp. 671–679.

[12] McMillin, B. K., Lee, M. P., and Hanson, R. K., "Planar Laser-Induced Fluorescence Imaging of Shock-Tube Flows with Vibrational Nonequilibrium," *AIAA Journal*, Vol. 30, No. 2, 1992, pp. 436–443.

[13] Roe, P. L., "Approximate Riemann Solvers, Parameter Vectors, and Difference Schemes," *Journal of Computational Physics*, Vol. 43, No. 2, 1981, pp. 357–372.

[14] Anderson, W. K., Thomas, J. L., and van Leer, B., "Comparison of Finite Volume Flux Vector Splittings for the Euler Equations," *AIAA Journal*, Vol. 24, No. 9, 1986, pp. 1453–1460.

[15] Wilcox, D. C., "Reassessment of the Scale Determining Equation for Advanced Turbulence Models," *AIAA Journal*, Vol. 26, No. 11, 1988, pp. 1299–1310.

[16] Wilcox, D. C., "Dilatation-Dissipation Corrections for Advanced Turbulence Models," *AIAA Journal*, Vol. 30, No. 11, 1992, pp. 2639–2646.

[17] Anderson, J. D., *Computational Fluid Dynamics*, McGraw–Hill, New York, 1995, pp. 301–303.

[18] Carroll, B. F., and Dutton, J. C., "Multiple Normal Shock Wave/Turbulent Boundary-Layer Interactions," *Journal of Propulsion and Power*, Vol. 8, No. 2, 1992, pp. 441–448.

[19] Liepmann, H. W., and Roshko, A., *Elements of Gasdynamics*, Dover, New York, 1957, Chap. 4.

R. So
*Associate Editor*